JM3 Journal of Micro/Nanopatterning, Materials, and Metrology

RESEARCH PAPER

Suitability of half-wavelength contact acoustic microscopy to detect deeply buried voids

Benoit A. J. Quesson,[a,*] **Douwe M. van Willigen**,[b] **Lars Hörchens**,[a] **Anne Maaike Gerritsma**,[a] **Marta Saccher**,[a] **Janusz Bogdanowicz**,[c] **Cong Chen**,[c] and **Paul L. M. J. van Neer**[a]

[a]TNO, Department of Acoustic Measurement Systems, Hague, The Netherlands
[b]TNO, Department of Optomechatronics, Delft, The Netherlands
[c]IMEC, Leuven, Belgium

ABSTRACT. **Background:** A key challenge in semiconductor 3D integration is the occurrence of small voids with diameters ranging from a few nanometers to several micrometers. Depending on the chip/package design and production process, these voids may occur across a large depth range (1 to 1000 μm)—e.g., the typical bond interface depth in wafer-to-wafer bonding lies at a depth of 775 μm. The standard tools to detect these deep defects are infrared microscopy, scanning acoustic microscopy (SAM), and X-ray. However, they all have limitations in resolution or penetration.

Aim: Here, we propose an acoustical technique named half-wavelength contact acoustic microscopy (HaWaCAM®) to sidestep this problem. HaWaCAM® consists of a 4 GHz transducer integrated on top of a custom-designed probe and uses solid-to-solid contact to couple waves into the sample, enabling a higher detectability and resolution compared with SAM.

Approach: In this work, we investigate the suitability of HaWaCAM® to detect deeply buried voids. We used the HaWaCAM® setup on a silicon wafer sample containing programmed voids of different sizes buried below 49 μm of silicon.

Results: We show that HaWaCAM® successfully detects voids down to a width of 0.75 μm at a depth of 49 μm. The signal-to-noise ratio varied from 30 to 45 dB, 20 to 30 dB, and 15 to 30 dB for void widths of 2.5, 1, and 0.75 μm, respectively.

Conclusions: We demonstrate the capability of HaWaCAM® to detect voids buried at large depths. We expect the current HaWaCAM® setup to detect voids with 2.5 μm widths with 6 dB SNR buried below >800 μm of silicon.

 [DOI: 10.1117/1.JMM.25.2.024001]

Keywords: acoustics; GHz acoustic metrology; half-wavelength contact acoustic microscopy; HaWaCAM®; voids; defects; subsurface

Paper 26004G received Jan. 12, 2026; revised Mar. 31, 2026; accepted Apr. 6, 2026; published May 5, 2026.

1 Introduction

Semiconductor 3D heterogeneous integration allows for the integration of different functionalities of separately manufactured components into a higher-level assembly, resulting in smaller volumes and better performance. As an example, the integration of memory, CPUs, or GPUs in a chiplet reduces bus line lengths, optimizes data exchange, and results in an overall increase in computation performance. Although hybrid bonding of die-to-wafer or wafer-to-wafer allows for

*Address all correspondence to Benoit A. J. Quesson, benoit.quesson@tno.nl

heterogeneous integration, air or void inclusions of a few nanometers to several micrometers are known to occur at the bonding interfaces. These defects can degrade the functionality of the final device by locally generating extra heat and potentially resulting in the disruption of the electrical contact. Given the typical 300 mm wafer thickness of 775 μm, these defects can be located at depths down to 775 μm or more.

Traditional inspection and metrology techniques all suffer from limitations in terms of penetration depth, detectability, lateral and vertical resolution, and throughput.[1] The detectability represents the minimum void size producing a measurable echo, as documented in this article, and the resolution represents the minimum lateral or vertical spacing for which two targets remain separable. The detectability depends on the SNR and frequency bandwidth, whereas the resolution depends mainly on the frequency (assuming the scan grid spacing is scaled accordingly). The techniques traditionally used for sub-surface inspection and metrology for depths down to a few micrometers are X-ray microscopy, infrared microscopy (IM), and scanning acoustic microscopy (SAM).[2,3] Optical-based solutions (microscopy, interferometry, etc.) and electron-based solutions (scanning electron microscopy: SEM) are all limited in penetration depth.[3] Photoacoustic metrology is also being developed but is limited in lateral resolution and is dependent on the sample surface material. A short description and overview of the performance and limitations of these different techniques is provided below.

In X-ray microscopy, the radiation beam generated by a source traverses the sample under test and is then detected by one or more X-ray detectors. The image is formed by varying the angle of incidence between the sample under test and the detectors. As different materials absorb radiation differently, defects such as voids or cracks can be detected in the resulting image through variations in contrast.[2,4,5] For the programmed voids in silicon samples as investigated in this article (see sample description in Sec. 3), it is expected that the density variation from the micrometer order voids or less is very small and would require very long exposure times.

IM takes advantage of the fact that silicon is transparent to wavelengths longer than 1.1 μm.[6] Using a laser with a suitable wavelength, it is possible to image through a wafer using a microscope combined with an infrared camera.[7,8] It was for instance reported that when two wafers were bonded with an oxide layer of 5 nm, one wafer as a cap wafer and the second wafer patterned with artificial voids with different etched depths, square voids 0.5 μm and 1.2 μm thick could be detected through the 775 μm capper wafer, transparent for the IR wavelength used.[8,9] However, the lateral resolution of this technique is inversely proportional to the imaging depth. Therefore, it is possible to image at larger depths up to the thickness of a silicon wafer at the price of a lower resolution.[1,8,9] As an example, for the 49 μm thick silicon sample with programmed voids studied in this paper, the smallest detectable void size with IM was found to be 2.5 μm.[1] However, in cases where bonding voids occur between metal interconnections, the infrared light will be reflected by the metal, limiting the penetration depth.[10]

Alternatively, chip or wafer inspection can be performed using acoustic waves. SAM is a well-established technique,[11] which allows for the nondestructive imaging of defects using ultrasound. It consists of a focused high-frequency transmitting transducer, which is coupled to the sample under investigation via a focusing lens and a liquid medium (usually deionised water). SAM operates as follows: a pulse is generated by the transmitting transducer, which travels through the coupling medium and through the sample, and interacts with the internal structures. The reflected sound waves are then detected again by the same transducer, now working as a receiver. Typical center frequencies of the transmitting transducer are in the range 100 MHz to 1 GHz, with the most common around 100 to 300 MHz. The resolution of this technique is proportional to the frequency. However, even if the propagation losses in the sample are linearly proportional to the frequency, the imaging depth is limited by the propagation losses in the coupling medium, which increases proportionally to the square of the frequency. The attenuation in a pure water couplant reaches, for pulse-echo, 44 dB/μm at 10 GHz. Due to the need for the acoustical lens, the acoustical path between the transducer and the sample is relatively long, posing constraints on the resolution and penetration depth. At frequencies below 500 MHz, the minimum detectable size of defects such as voids is 5 to 10 μm at depths ranging down to 2 mm.[12–14] The contrast in the resulting image is caused by the reflection induced by the acoustic impedance differences along the path travelled by the ultrasound pulse. This technique is therefore very sensitive in detecting voids or delamination while being less sensitive to the presence of metallization on the sample under investigation. In addition, it does not require sample preparation, but it is limited by the need for a coupling medium. Furthermore, this limits the ease of integration into chip fabrication process flows.[6]

A second acoustical technique is photothermal imaging. Photothermal imaging relies on the absorption of optical energy in the sample, which causes fast localized heating of the material, generating an expansion and a mechanical wave that propagates through the material, in a similar fashion as in SAM.[15–17] In contrast to SAM, however, the pulse is very broadband and can reach tens and even hundreds of GHz.[16,17] In reception, to create an image of the sample under test, the void echoes can be detected using a laser interferometer. The axial resolution represents the resolution along the depth axis. For this technique, it is in the order of hundreds of nm, limited by the maximum acoustic frequency, for a lateral resolution in the order of a few micrometres, limited by the diameter of pump or readout beam. The group of Chen[18] reported a lateral resolution of 2.3 μm at a depth of 100 μm, and the group of Gao[3] reported that using a femtosecond laser able to excite the third and fifth optical harmonics, they were able to improve the lateral resolution to 1 μm with an axial resolution of 121 nm. However, this technique suffers from several drawbacks: the optical to mechanical energy conversion is sample-dependent, which means the produced acoustic frequency and amplitude are sample-dependent as well. The very large bandwidth could lead to aliasing during data acquisition if the sampling frequency is not high enough. In addition, the optical energy, which can be deposited, is limited by the risk of thermal damage to the sample.

To sidestep some of the challenges described above, here, we propose a new acoustics-based technique called half-wavelength contact acoustic microscopy (HaWaCAM®) and explore its suitability to detect deeply buried voids (>10 μm deep).

2 Methods

2.1 HaWaCAM® Concept

HaWaCAM® consists of a custom-designed probe with a GHz piezoelectric transducer integrated above a silicon tip. The need for a liquid coupling is substituted by a solid tip-to-sample contact.

By doing so, the attenuation in the coupling layer competes with the reflection and transmission coefficients at the tip-sample interface to the benefit of the solid tip-sample contact. As explained in the introduction of the SAM technology, the extreme attenuation values in the coupling layer in the GHz frequency range do not allow for enough energy to be transmitted to the sample. This allows for the use of much higher acoustic frequencies compared with SAM, resulting in higher axial resolution. Other parameters may influence the tip-sample contact coupling efficiency, such as the contact area, the sample material, or the roughness; these are further discussed in Sec. 4. The probe is scanned across the surface of the sample under investigation. The echoes of the subsurface voids are recorded by the same GHz transducer, aggregated and saved for further processing (Fig. 1).

A GHz acoustical pulse (typically a linear chirp) is generated by the piezo transducer and travels linearly through the tip and sample. The diameter of the GHz transducer and the tip height are designed such that the transducer's natural focus lies at the tip-sample interface. At the

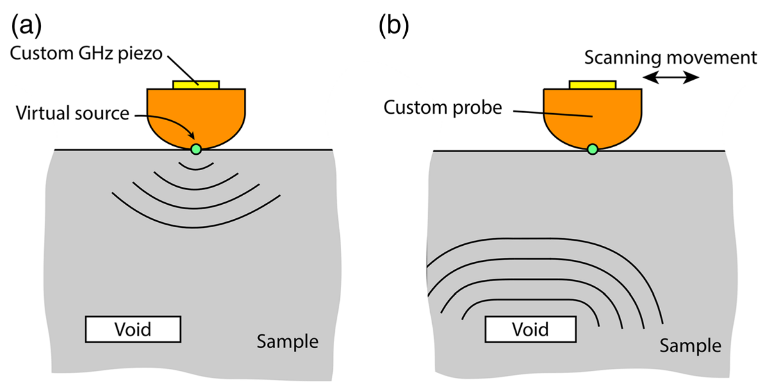

Fig. 1 Schematic image showing the Half-Wavelength Contact Acoustic Microscopy (HaWaCAM®) inspection concept in emission (a) and reception (b).

transducer focal distance, the amplitude benefits[19] from a factor of 2, and at the same time, the focusing limits the reverberation in the tip.

The tip-sample contact radius a can be calculated using an approximation based on Hertzian mechanical contact theory for a solid sphere pressing onto a solid half space,[20] governed by $a^3 = 3FR/4E^*$ and $1/E^* = (1-\nu_t^2)/E_t + (1-\nu_s^2)/E_s$, where F is the downward vertical force applied on the probe (approximated here as a sphere), R is the equivalent tip radius (sphere), and E^* is the reduced Young's modulus obtained from the elastic moduli E_t and E_s, and the Poisson ratios ν_t and ν_s of the tip ($_t$) and sample ($_s$), respectively. The tip-sample contact area acts as an acoustical "slit" and determines the energy transfer efficiency from tip to sample and vice versa. Moreover, in transmission, the tip-sample contact area acts as an acoustic source on top of the sample and hence determines the directivity pattern produced in the sample (green disks in Fig. 1). When the tip-sample contact diameter is small compared to the wavelength (e.g., $<1/2$ wavelength), the opening angle of the induced compressional wave is large. At larger contact radii, the opening angle reduces. For contact radii below λ/π, the effective acoustic impedance of the tip-sample interface becomes complex for the waves passing through this interface, which means the real part of the transmission coefficient at the tip-sample interface reduces. This implies that more energy is reflected back to the transducer. To prevent damage to the sample or the probe, the contact force in combination with the probe tip shape should result in a peak contact stress below the compressive strength of the sample surface material. In practice, for both silicon and PMMA, it is possible to reach a contact diameter of $\lambda/2$ or more without damaging the sample with the current probe tip shape.[21] The acoustic wave travels from the virtual acoustic source at the tip-sample interface downward. If it encounters a scatterer, some acoustic energy is reflected back toward the sample surface. In reception, the tip-sample interface acts again as an acoustic "slit" forming a virtual source in the probe tip. The wave travels further through the tip and is received by the GHz piezoelectric transducer mounted on top of the probe.

2.2 HaWaCAM® Experimental Setup

A custom HaWaCAM® setup was developed and implemented.[21,22] The probe contained a circular piezoelectric transducer (scandium-doped aluminum nitride, 4 GHz center frequency, −6 dB bandwidth 28%, 24 μm diameter) mounted on top of a custom-designed cantilever (length × width × thickness of $2 \times 0.2 \times 0.03\ \mathrm{mm}^3$) with a blunt tip (radius > 10 μm, height ~80 μm). A picture of a HaWaCAM® probe and a scanning electron microscope zoom around the transducer are visible in Fig. 2.

Scans using the HaWaCAM® setup were made of the sample under test on a number of regions containing different void widths, described in Sec. 4. For each scan point, 400 pulse-echo time traces were recorded and averaged. The applied static force to the probe was ~800 μN to maintain a $\lambda/2$ tip-sample contact diameter and thus a point source at the tip-sample interface, as explained in Sec. 2. For the HaWaCAM setup, assuming $F = 800$ μN, a Young modulus E of 70 GPa, a Poisson ratio of 0.28 for Si, and an equivalent tip radius of 10 μm, the contact diameter is 1 μm, which is close to $\lambda/2$. This ensured a large field of view and enabled the use of imaging algorithms. An arbitrary waveform generator (AWG, Keysight M8195A, Santa Rosa, California, United States) was used to generate the signals (linear chirps, center frequency 4 GHz, bandwidth 8 GHz), which were amplified (gain of 28×, ZVA-183WX-S+, Mini-circuits, New-York, United

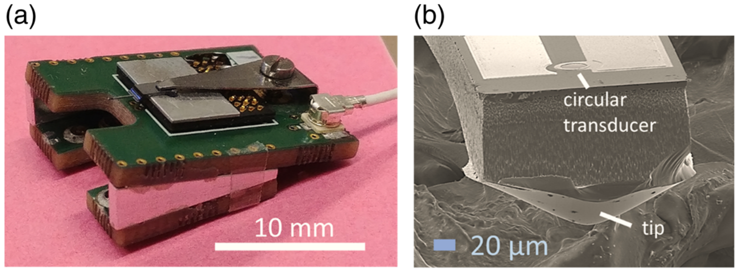

Fig. 2 HaWaCAM® probe mounted on a probe holder (a). Scanning electron microscope image of the end of the HaWaCAM® probe with the 24 μm diameter transducer and 80 μm high tip visible (b).

States) and subsequently used as input on the HaWaCAM® transducer located on top of the probe. In reception, the signals were amplified by a factor of 30× (LNA-30-00101200-17-10P, Narda-MITEQ, New York, United States) and digitized by an oscilloscope (Tektronix DPO75002SX, Beaverton, Oregon, United States) at a sampling rate of 25 GHz. A custom-designed pulse-echo switch allowed switching between transmit and receive chains within 15 ns. The HaWaCAM® setup was integrated in a modified atomic force microscope (Bruker dimension FastScan, Billerica, Massachusetts, United States) to enable positioning and 2D scanning and to control the static force applied on the probe.

2.3 Sample Description

A sample was fabricated consisting of a silicon wafer (thickness 775 μm) with air voids (nominal height 75 nm) buried below a nominal depth of 49 μm of silicon. The voids were grouped in regions, each containing a square matrix of square voids. The inter-region pitch was 2.8 mm, and the inter-void pitch was 40 μm. The voids in each region had a specific width, and the void width range in the sample was 10 nm to 20 μm. For a schematic image of the sample, see Fig. 3.

2.4 Signal Processing

The datasets were gathered along the x–y plane, which means that the datasets consisted of data cubes along $\{x, y, t\}$, with x and y being the two perpendicular scanning directions on the sample surface plane, and t representing the measurement time. The signal processing consisted of the following sequential steps:

- The time traces were matched-filtered by correlation with a recording of the pulse that was sent to the transducer. This step increases the signal-to-noise ratio of the coherent echoes in the time traces matching the sent pulse.
- The data were compensated for the jitter present in the trigger sent by the AWG. This operation was performed by calculating the trace-by-trace time shift of the trigger signals using cross-correlation and time-shifting the received pulse-echo signals using the appropriate time delays. As one of the migration steps relies on the coherent summation of the data, it is important that the time jitter present in the trigger is not greater than half a wavelength at the maximum emitted acoustical frequency. For the maximum frequency of 8 GHz, this corresponds to ∼62.5 ps.
- Time windowing was applied by selecting a time window where all echoes from the voids are present. This time window is used to filter out the first micrometers of the sample where some artifacts from the tip-sample interface may be present, due to the presence of defects or particles, for instance. It is also used to reduce the data size and hence speed up the migration step.
- Time interpolation by an oversampling factor of 10.
- Image reconstruction was carried out by applying a Stolt migration.[23]
- A spatial filter was applied based on the expected minimum resolvable void size.

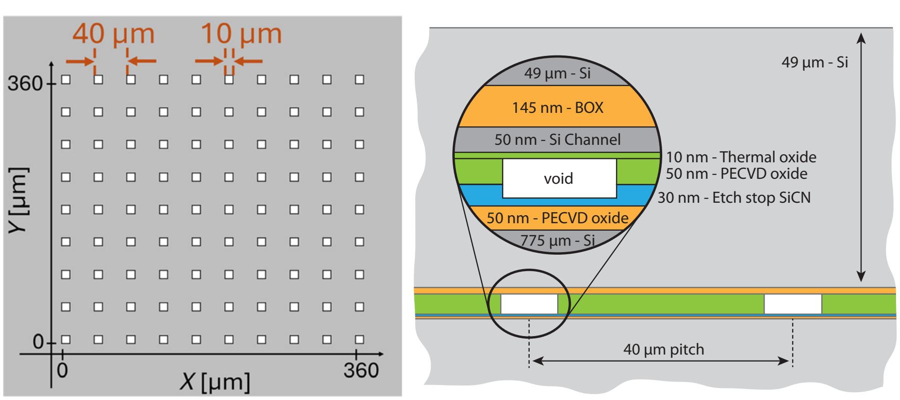

Fig. 3 Sketch of the programmed void sample layering stack, adapted with permission from Ref. 3. The nominal void height was 75 nm.

3 Results

Three scans were performed: one scan of $40 \times 40\ \mu m^2$ around a 2.5 μm void, a scan of $80 \times 80\ \mu m^2$ around four 1 μm voids, and a scan of $80 \times 80\ \mu m^2$ around six 750 nm voids. The results are presented in the next three subsections. The voids were identified by the time of flight corresponding to their expected depths, their expected positions: starting from a larger, easily identifiable void, and moving with the known x–y offsets to the smaller voids, and the known nominal 40 μm pitch between them for the scans with multiple voids.

3.1 Single 2.5 μm Void

A scan of $40 \times 40\ \mu m^2$ with 500 nm steps in both x and y directions was performed around the single 2.5 μm void expected position, resulting in a 3D data cube of $[80 \times 80 \times 1000]$ samples along x, y, and time, respectively. Figure 4 shows the schematic cross-sections of the sample geometry, highlighting important distances.

Figure 5 displays the sum of the matched filtered data time traces (received amplitude versus time) after jitter compensation, around the void location at $[x, y]$ location of [14 to 24, 17 to 27] μm^2 [x, y axes as displayed in Fig. 6(a)]. It shows features such as the tip-sample echo, and the expected time range of the voids echoes (orange box). The tip-sample echo does not have the highest amplitude in the time trace. Echoes coming later from the subsurface have a comparable or higher amplitude, which demonstrates the efficient solid to solid coupling of acoustical energy in the sample. The compressional speed of sound in the silicon sample was estimated using the time difference between the first void echo visible at $t = 15.47$ ns [Fig. 5(b), arrow a] and the tip-

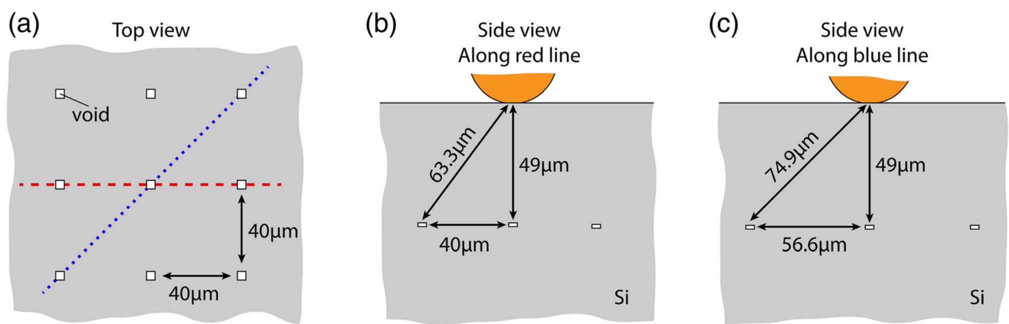

Fig. 4 Schematic cross-sections of sample geometry highlighting important distances. (a) Top view, (b) side view along the red dashed line, and (c) side view along the blue dotted line.

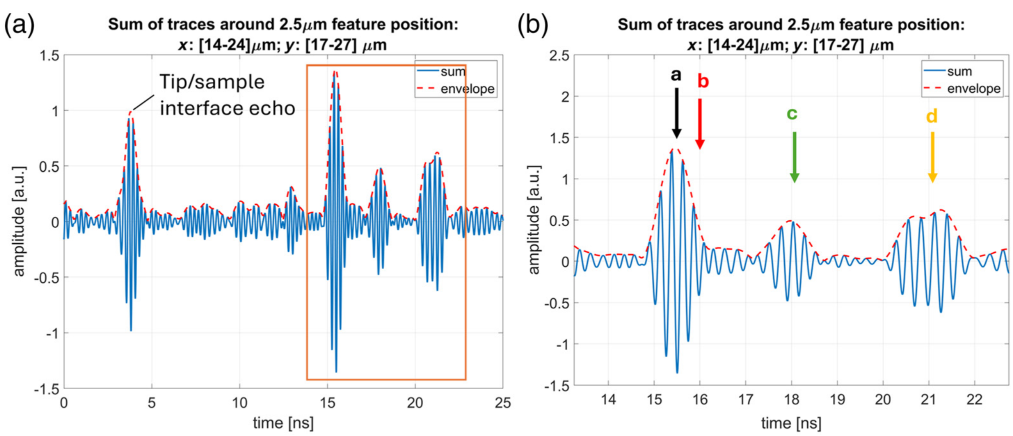

Fig. 5 (a) Sum of raw data time traces (received amplitude versus time) recorded in an $[x, y]$ window of [14 to 24,17 to 27] μm^2, indicating the tip-sample echo and the expected time range of the inclusion-echoes (orange box). (b) Zoom of the orange box in the example raw data time trace shown in panel (a). The letters and colored arrows refer to the time instances in the $[x, y]$ images presented in Figs. 6(a)–6(d).

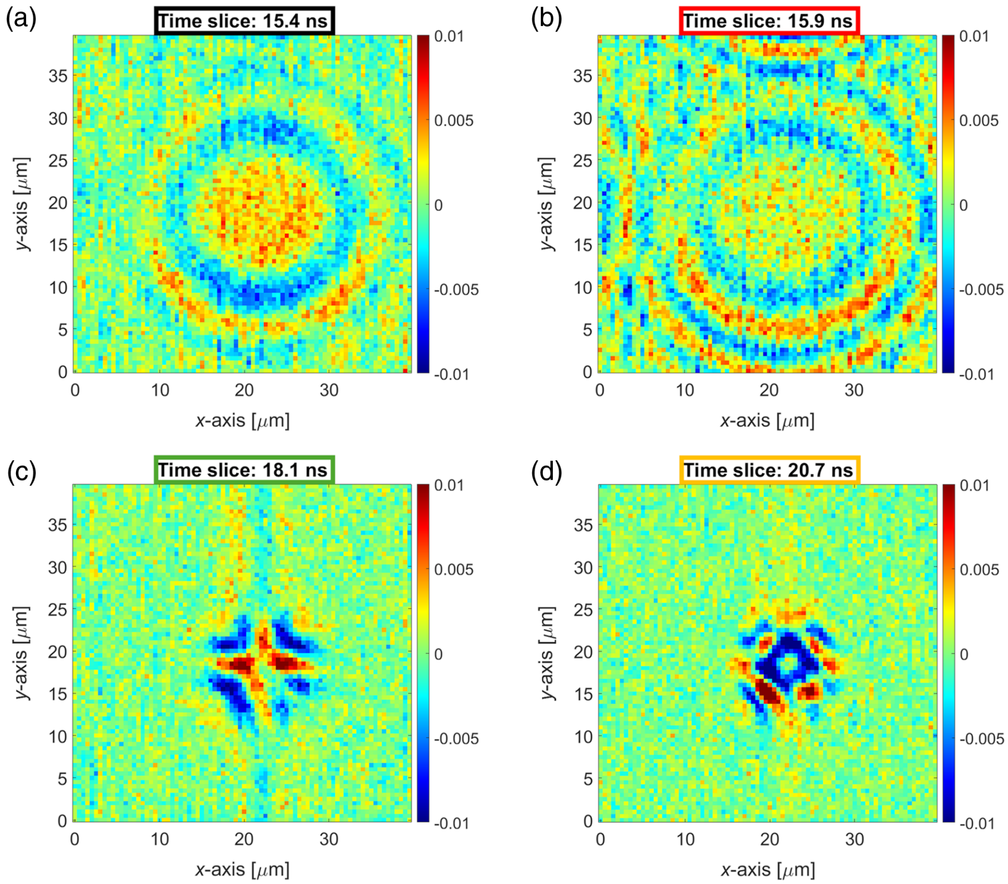

Fig. 6 2D crosscuts along $[x, y]$ of the acquired 2.5 μm void data prior to migration at a time slice of 15.4 ns (a), 15.9 ns (b), 18.1 ns (c), and 20.7 ns (d). The color scale indicates the signal level in arbitrary units.

sample interface echo visible at $t = 3.79$ ns [Fig. 5(a)], considering the data envelope (red curves in Fig. 5). This time corresponds to the two-way propagation in the sample down to the void; nominally 49.195 μm (Fig. 3, right hand side), considering the silicon, BOX and Si channel layers. This time difference corresponds to an estimated compressional sound speed of ~8420 m/s in silicon. This value is in line within 4% with the literature. Longitudinal speed of 8556 m/s or 8690 m/s is for instance reported for a ⟨100⟩ crystal orientation silicon wafer.[24] It was decided to proceed with the measured value as it was deemed more representative of the wafer under test. Figure 5(b) is a zoom corresponding to different subsurface echoes [time limits delimited by the orange box in Fig. 5(a)].

Figures 6(a)–6(d) display 2D crosscuts along $[x, y]$ of the data prior to the Stolt migration at time slice of 15.4, 15.9, 18.1, and 20.7 ns, respectively, corresponding to the different arrows displayed in Fig. 5(b).

Figure 6(a) shows the 2D $[x, y]$ crosscut image taken at 15.4 ns [at the time indicated by the black arrow in Fig. 5(b)]. Here, the maximum amplitude of the arrival of the direct echo is visible at 15.4 ns. Using the previously estimated compressional wave speed of 8420 m/s and correcting for the tip-sample echo maximum (at around 3.7 ns), the measured arrival time matches with the expected arrival time of 11.7 ns, corresponding to a depth of 49.3 μm. This closely matches the nominal design depth of 49.195 μm. In addition, the echo of the 2.5 μm square void has a spherical shape. This is caused by the fact that the 2.5 μm width of the square void is close to the acoustical wavelength in silicon at 4 GHz (~2.1 μm), resulting in limited resolution.

Fast-forwarding in time to the 2D $[x, y]$ crosscut image taken at a time of 15.9 ns shown in Fig. 6(b), one can observe not only the spherical waves produced by scattering off the primary inclusion but also spherical waves produced by neighboring inclusions to the left and top of the central defect (see also center schematics in Fig. 4). This is caused by the fact that the tip-sample contact area acts as a virtual source with a large opening angle.

Fast-forwarding again in time to the 2D $[x, y]$ crosscut image taken at a time of 18.1 ns displayed in Fig. 6(c), one can observe the interference of the echoes produced by neighboring inclusions located closest horizontally and vertically with respect to the central defect.

Likewise, the 2D $[x, y]$ crosscut image taken at a time of 20.7 ns displayed in Fig. 6(d) shows the interference pattern of the neighboring inclusions located diagonally (see right schematic in Figs. 6 and 4). The constructive interferences of the four voids placed laterally or diagonally [Figs. 6(c) and 6(d), respectively] produce a higher amplitude than the single void measurement at 15.4 ns, as expected.

Using the compressional wave speed within silicon, all the aforementioned travel times well match the actual sample geometry. Figure 7(a) shows the data after all the processing steps are applied for the same time slice at $t = 14.7$ ns. This time difference with the matched filtered and jitter compensated data was explained by the fact that the first echo arrival is hidden in the noise in the matched filtered data [Fig. 6(b)]. The migration algorithm resulted in a higher contrast for a speed of sound of 8500 m/s in silicon, close to the 8420 m/s estimated from the nonmigrated data. The void is clearly visible. Next to the main lobe at [22,19] μm, sidelobes are visible [white arrows in Figs. 7(a) and 7(b)]. These were caused by the rectangular tapering of the spatial domain before application of the migration algorithm. Figure 7(b) shows the same dataset but along an x-axis crosscut at $y = 18.5$ μm with respect to time. The void is visible with the same contrast and the processing side lobes as well. An additional feature was observed: around the void depth [around 49 μm in Fig. 7(b)], an increase in energy is visible along the whole x-axis length. This unexpected increase in scattered energy at locations without programmed voids may suggest inhomogeneities along the bonding interface at the void depth. This effect is also consistently visible for the smaller void datasets analyzed [Figs. 8(b)–8(c) and Figs. 9(b)–9(c)], which suggests that this effect is not localized but distributed over a larger area. No voids were visible in the other slices of the data cube. The tip-sample echo was clearly visible in the first 1 to 2 μm of the top sample surface as a local increase in amplitude. The measured void size was measured on the fully processed data and was estimated at 3×2 μm^2, which is different from the nominal void size of 2.5×2.5 μm^2.

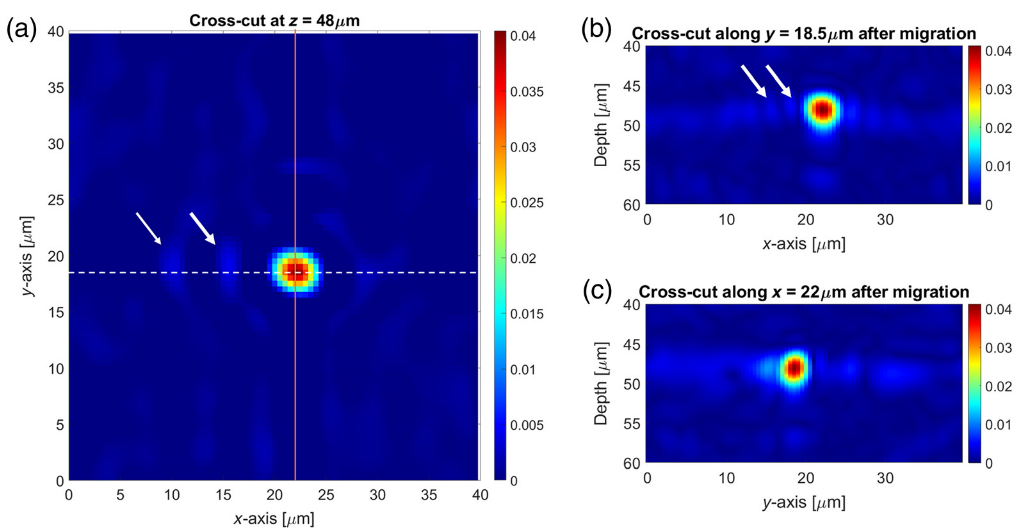

Fig. 7 (a) Fully processed result for the 2.5 μm void, slice at $z = 48$ μm, assuming a sound speed of 8420 m/s. (b) Cross cut along x-axis and $y = 18.5$ μm for the same dataset, corresponding to the white dotted line in panel (a). (c) Cross-cut along the y-axis and $x = 22$ μm for the same dataset, corresponding to the orange dotted line in panel (a). For panels (a), (b), and (c), the color scale indicates the intensity from 0 to the maximum in the image in arbitrary units. Side lobes created by a rectangular tapering in the wavenumber algorithm are visible (e.g., at the white arrows location).

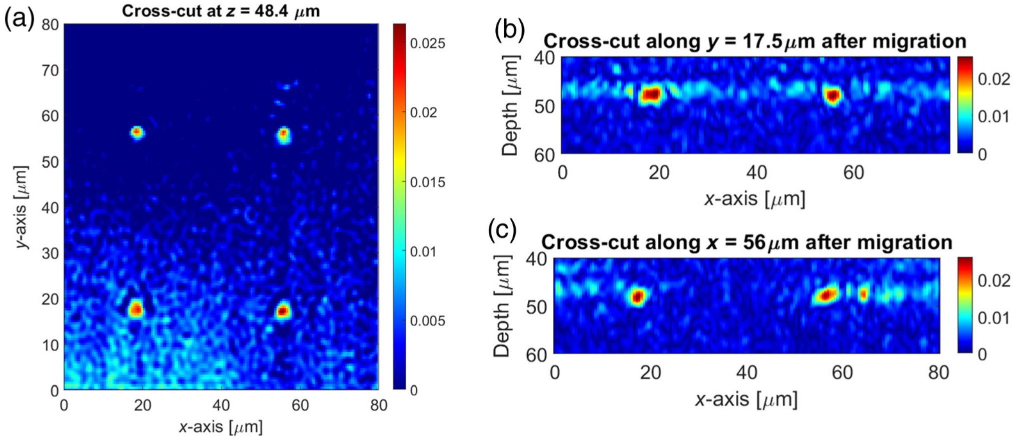

Fig. 8 Fully processed result for the four 1 μm voids, (a) slice at $z = 48.4$ μm assuming a sound speed of 8420 m/s. (b) Cross-cut along x-axis and $y = 17.5$ μm for the same dataset, corresponding to the white dotted line in panel (a). (c) Cross-cut along y-axis and $x = 56$ μm for the same dataset, corresponding to the orange dotted line in panel (a). For panels (a), (b), and (c), the color scale indicates the intensity from 0 to the maximum in the image in arbitrary units.

3.2 Multiple 1 μm and 750 nm Voids

Figure 8 shows the fully processed measurement results for four square voids of size 1×1 μm^2 [see Fig. 8(a), at locations [18.5, 56.5], [18.5, 17.5], [55, 17.5], and [55, 56.5] μm]. The figure also shows that the noise locally increases at the depth of the voids [Figs. 8(b) and 8(c)]. However, it is not uniformly distributed along x-y [Fig. 8(a)]. The consistent local increase in scattered energy corresponding exactly to the voids depth but where no void or feature is expected suggests inhomogeneities in the bonding process. Inhomogeneities for silicon to silicon wafer bonding are well documented;[25] they can originate from the surface roughness or bow of the wafer surfaces to be placed in contact, the introduction of particles or trapped water or gas at the interface, or stress-induced debonding. These suspected inhomogeneities could potentially lead to data misinterpretation, especially for smaller voids where the echo amplitudes are weaker: As an example, two higher amplitude echoes are visible around $y = 60$ μm in Fig. 8(c): one just before 60 μm and one just after. The echo before $y = 60$ μm is associated to the void because the pitch is assumed constant and the two voids visible in Fig. 8(b) are located at the same positions along the x-axis. However, more evidence and supporting measurements are necessary to support and validate this hypothesis; this is a research direction that would require more attention as it could potentially provide valuable insights into the bonding processes.

Figure 9 shows the fully processed measurement results for six square voids with a width of 0.75 μm [see Fig. 7(a), at locations [1, 28.5], [0.5, 67], [36.5, 28], [36.5, 68], [74, 27.5], and [74.5, 66] μm].

An unknown defect, centered at around [50,60] μm is visible in Fig. 9(a). It is likely associated with a dent or particle present on the surface of the sample (visible in the raw and processed data, not displayed here). From the results in Fig. 9(a), it can be seen that the void pitch is closer to 35 μm rather than the nominal pitch of 40 μm. This difference cannot be fully explained and could be attributed to a systematic error in the scanning stage. More data would need to be gathered to come to a conclusion. In addition, the 750 nm void data show a local increase of noise at the void depths attributed to bonding inhomogeneities, as for the 1 μm void data. This is particularly visible in Fig. 9(c), whereas in Fig. 9(b), it is less visible, which seems to confirm the spatial dependency. It should be noted that this effect is also visible to some extent for the 2.5 μm void scan [Figs. 7(b) and 7(c)], but less noticeable in this dataset because of the larger dynamic range due to the larger amplitude of the 2.5 μm void.

3.3 Void Sizes and Signal-to-Noise Ratios

The signal-to-noise ratio was computed as the ratio of the maximum void-echo amplitude over the typical noise amplitude as described below. The noise was computed by selecting a noise/clutter-free area. An overview of the maximum and noise areas for the three datasets is available in Table 1.

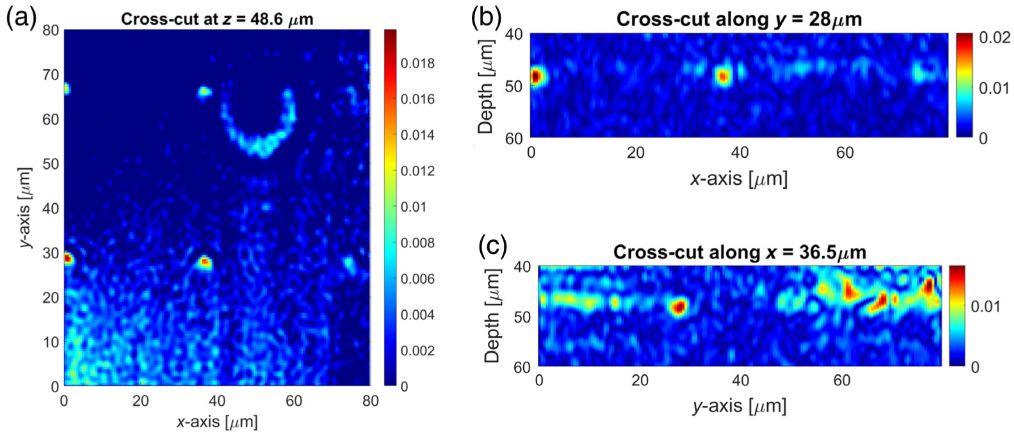

Fig. 9 Fully processed result for the six 750 nm voids, (a) slice at $z = 48.6$ μm assuming a sound speed of 8420 m/s. (b) Cross-cut along x-axis and $y = 28$ μm for the same dataset, corresponding to the orange dotted line in panel (a). (c) Cross-cut along x-axis and $y = 67.5$ μm for the same dataset, corresponding to the white dotted line in panel (a). The three white arrows correspond to the three 750 nm voids in panel (a). The last one at $x = 74.5$ μm is not visible in panel (a) but visible in panel (c) because of a difference in depth of about 1 μm. For panels (a), (b), and (c), the color scale indicates the intensity from 0 to the maximum in the image in arbitrary units.

Table 1 Location of void and noise areas for the different scans.

Feature size [μm]	Max location [x, y] in [μm]	Noise reference area location in [μm] [x_{min}–x_{max}, y_{min}–y_{max}]
2.5	[22, 19]	[0 to 15, 25 to 39]
1	[55, 17.5]	[60 to 80, 25 to 50]
0.75	[36.5, 28]	[60 to 80, 30 to 45]

As the clutter noise is not uniform because of the local bonding contribution as observed previously, an SNR bracket is provided rather than one value. The noise level is computed as follows: a distribution of the noise amplitude in 50 bins in the selected noise/clutter area is computed. The noise amplitude with the maximum number of occurrences is selected as reference, and it corresponds to the most occurring noise/clutter value A. From this baseline, a noise amplitude bracket is selected corresponding to 50% of the maximum number of occurrences below and above the value A. The corresponding noise values are then converted to decibels.

The signal-to-noise ratio after processing was 30 to 45 dB for the 2.5 μm void, 20 to 30 dB, and 15 to 30 dB for the 1 and 0.75 μm void size, respectively. The SNRs and measured void sizes are summarized in Table 2.

Table 2 Programmed and measured inclusion widths and associated SNR.

Void size [μm]	Void size [λ[a] ratio]	x–y measured sizes along x–y [μm]	Void depth [μm]	SNR [dB]
2.5	1.2 λ	3 to 2.5	50	30 to 45
1	0.5 λ	2.1 to 2.1	49.5	20 to 30
0.75	0.35 λ	2.1 to 2.1	50	15 to 30

[a]Assuming a reference wavelength $\lambda = 8420/4$ GHz $= 2.1$ μm.

4 Discussion

The estimated imaged size of the square voids with a programmed width of 1 μm [see Fig. 8(a)] is $2.1 \times 2.1\ \mu m^2$. It is similar to the estimated imaged size of $2.1 \times 2.1\ \mu m^2$ of the square voids with a programmed width of 0.75 μm [see Fig. 9(a)]. These imaged sizes are close to the acoustic wavelength—∼2.1 μm in Si at 4 GHz—rather than their actual programmed width. This is caused by the combination of acoustical wavelength and limited scan size. By increasing the scan size, the imaged size of the voids could approach the theoretical resolution limits of half an acoustic wavelength (∼1.1 μm). However, to get to this resolution, the SNR of the void would need to be at least 6 dB after accounting for the losses due to attenuation and diffraction in the sample for these larger ranges. In the regime where the void dimensions are close to the acoustical wavelength, resonances and interferences may occur. For the defects under investigation in this article, the void target thickness is 75 nm, which is ∼0.03 times the wavelength (λ). The acoustical field being mainly compressional in nature, it is expected that the vertical shape of the voids will not affect the target response, besides their equivalent air volume.

Moreover, the same inclusions were measured by Chen et al.[1] using a commercial off-the-shelf SAM with a frequency of 175 MHz and IM. The smallest detected single voids with these technologies and HaWaCAM® are summarized in Table 3.

Table 3 shows that the HaWaCAM® setup was able to detect 10× smaller voids compared with SAM and 3.3× smaller voids compared with IM on the same sample type. Assuming a 6 dB detection limit is deemed sufficient for void detection, as is commonly used for detectability in SAM,[26] and that the defects behave as incompressible spherical scatterers, we expect the current HaWaCAM® setup to be able to detect defects with widths down to a size of 0.4 μm at 49 μm depth. This would be an improvement of 18.8× and 6.25× compared with the SAM and IM cases, respectively.

Next to extrapolating the HaWaCAM® performance to smaller defect sizes, one may also extrapolate said performance to larger depths. Taking into account the additional attenuation and diffraction effects, we expect air inclusions of width 2.5 μm to be detectable at depths larger than 800 μm using the current experimental setup. We expect that the performance of the HaWaCAM® system could still be improved further by improvements in the transducer design, electronics, and signal processing.

An overview of different metrology and inspection techniques for deeply buried defects and their performance with respect to the smallest detectable void size and detection depth was proposed by IMEC[1] and shown in Fig. 10. The figure was modified to include HaWaCAM® based on the results presented and extrapolated in this article. The results presented in this article are displayed as three black dots in Fig. 10, corresponding to the void size and depths as listed in Table 2. The black plus symbol (+) corresponds to the 400 nm defect size extrapolation at 49 μm discussed in this section and reported in Table 3. The black X symbol (×) corresponds to the 2.5 μm defect extrapolation to 800 μm depth, as discussed in this section. The larger area corresponds to variations expected from higher or lower center frequencies. As can be seen, HaWaCAM® is a viable technique toward achieving smaller defect detection capabilities at larger penetration depths (green X symbol in Fig. 10). Besides the resolution and penetration, the throughput is an important aspect to consider for the applicability of the method. However, the throughput values presented in Fig. 10 are only indicative as they depend, among other things, on the scan area and step size for the different techniques. The attenuation model used for the extrapolation to larger depths assumes an attenuation[27] of 1000 dB/m/GHz, following a linear relationship with frequency. According to the literature,[28,29] the attenuation in bulk silicon

Table 3 Programmed and measured inclusions widths and associated SNR.

	Smallest measured single void (μm)
Scanning acoustic microscopy—175 MHz[1]	7.5
Infrared microscopy[1]	2.5
HaWaCAM—4 GHz (measured)	0.75
HaWaCAM—4 GHz (extrapolated, current setup, 6 dB detection limit)	0.40

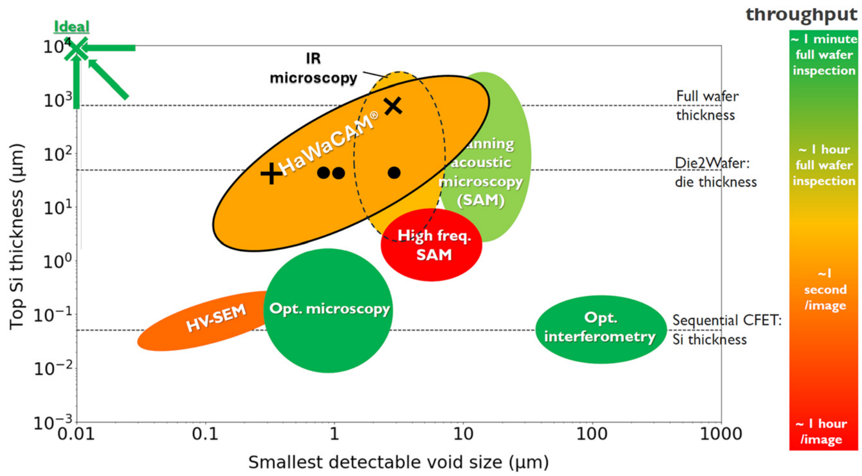

Fig. 10 Overview of inspection and metrology techniques for 3D integration, adapted with permission from Chen et al.[1] with the addition of HaWaCAM® (encircled with a solid black line). Measurements presented in this article as black dots. Extrapolations along smallest detectable void size for a fixed 49 μm depth and an SNR of 6 dB (+). Extrapolation along depth for a fixed void size of 2.5 μm and an SNR of 6 dB (×). The throughput values are only indicative as they depend, among other things, on the scan area and step size for the different techniques.

depends on crystal orientation and frequency: in ⟨111⟩ crystal-oriented Si, higher attenuation is observed than in ⟨100⟩ crystal-orientated Si. There is a regime change between the low and high GHz range in frequency: typically around 800 to 900 MHz for ⟨100⟩ or 8 to 9 GHz for ⟨111⟩. Below this frequency, the relation to attenuation is quadratic, and above this frequency, the frequency relationship becomes linear. As we consider 4 GHz and a ⟨100⟩ oriented Si wafer, the linear approximation is justified in that context.

As compared to SAM, which is available commercially and is also an acoustics-based technology, HaWaCAM® benefits from a few advantages: SAM necessitates scanning along depth because an acoustic lens is used, which removes one degree of freedom. In addition, as HaWaCAM® is probe-based, the option to multiplex the scanning on multiple areas can be considered. Another major difference with SAM is the fact that the tip for HaWaCAM® is in contact with the sample and does not need a coupling. This solid-solid tip-sample interaction leads to three consideration points:

- Damage: It should be noted that the force applied to the probe is present only to maintain the tip-sample contact diameter and not to exercise pressure on the sample. For a typical static force of 800 μN, as used during the measurements, the contact area via Hertz theory,[19] is about 860 nm for a HaWaCAM® probe. The equivalent pressure is therefore $P = 800\ \mu\text{N}/\pi a^2 \sim 1.4$ GPa. The pressure exerted by the HaWaCAM® probe is therefore in the same range as the pressure exerted by a typical AFM cantilever. For an AFM cantilever, due to the nanometric contact area between the AFM tip and the surface, normal forces of only a few nanonewtons result in local contact pressures in the gigapascal range.[30] As the pressure applied is limited, it is expected that the end of tip integrity is preserved and that contamination is limited; however, more tests and measurements are needed to characterize and validate this hypothesis under specific conditions.
- Roughness: Another aspect of the solid-solid tip sample contact that may be considered in a dedicated study is the efficiency of the acoustical energy transfer due to the roughness of the sample in comparison to the acoustical wavelength. It is especially relevant for backend or packaging use cases where the sample roughness is typically larger. For the measurements presented in this article, the roughness was not characterized, but the wafer was not polished. Unpolished silicon wafers can have roughness ranging from 100 nm to a few micrometers. The HaWaCAM® setup used a modified AFM to control the static force applied to the cantilever. This ensures that there is a maximum in the applied static force such that no plastic deformation/damage occurs. As the probe tip touches and is pressed into the surface, the peaks of the roughness are compressed. Variations in the distribution

Table 4 Tip-sample interface amplitude efficiency for several sample materials.

Sample material	Density [kg/m^3]	Longitudinal speed of sound [m/s]	Pulse-echo amplitude efficiency at tip-sample interface
Si	2500	8420	1
SiO_2	2200	5800	0.94
GaAs	5300	5000	0.99
GaN	6150	5800	0.89
Cu	8900	2500	0.99

of the height, density, and shape of the roughness peaks as a function of the location on the sample mean that, at the maximum static force, the height (z) at particular (x, y) locations of the tip-sample interface may vary. As the tip-sample interface acts as a virtual source, this means that the heights (z) of the (x, y) scan grid of virtual sources vary. The imaging algorithm applied (Stolt migration) assumes uniform sampling. Depending on the distribution of the height (z) variation of the virtual sources, this could lead to suboptimal collapse of the diffraction hyperbolas into the reflector shape (i.e., a worse resolution) or lead to speckle-like artifacts. Both effects are visible in the results shown in Figs. 7–9, but it is difficult to be 100% certain that these effects are solely caused by the aforementioned causes. Despite this, voids could be detected that were smaller than the performances provided by commercial off-the-shelf techniques (SAM and IR microscopy).

- Transmission efficiency: the half-wavelength virtual source diameter at the tip-sample interface varies with the sample material according to $\lambda = c/f$, with c the compressional sound speed in the sample material. The corresponding amplitude generated scales with the area of the virtual source and hence with the square of the virtual source radius in the far field. This is the main loss factor; however, it can be compensated for by the application of a larger static force and hence contact diameter within the maximum yield stress allowed by the sample material before damage appears. Exact characterization of this parameter should be performed in a follow-up study. In addition, the tip-to-sample and sample-to-tip transmission coefficients are sample material dependent and related to the acoustic impedance of the tip and sample. Assuming plane waves as a first-order approximation, the transmission efficiency in amplitude is defined as $T = 2Z1/(Z1 + Z2)$, with $Z1$ and $Z2$ the acoustical impedances of the input and output materials, respectively, and $Z = \rho \cdot c$ with ρ and c the density and the longitudinal speed of sound of the material under consideration, respectively. The total correction is defined as the product of the tip-to-sample transmission times the sample-to-tip transmission coefficients. Table 4 provides some numbers for typical sample materials. As can be seen in this table, for the considered sample materials, the pulse-echo efficiency at the tip-sample interface due to material property variation varies by ∼1 dB (10%).

5 Conclusion

In this work, we have introduced a new acoustics-based technique called Half-Wavelength Contact Acoustic Microscopy (HaWaCAM®) and experimentally showed that it is able to detect deeply buried voids. Voids with widths down to 0.75 μm buried below 49 μm silicon were detected. This was found to be between 10× and 3.3× smaller compared with commercial off-the-shelf SAM and IM, the latter being limited by penetration in metal layers. Moreover, extrapolating these results, we expect to be able to detect defects down to 0.4 μm widths buried below 49 μm silicon, or to detect 2.5 μm defects buried below 800 μm silicon.

Disclosures

Some of the authors of this article are listed as inventors to one or more not yet published patent applications that are relevant to the subject matter discussed in this article.

Code and Data Availability

Data underlying the results presented in this paper are not publicly available at this time but may be obtained from the authors upon reasonable request.

Acknowledgments

The authors acknowledge gratefully the contribution of Linda Feenstra for her mechanical design work and support with the wafer holder.

References

1. C. Chen et al., "Detection of bonding voids for 3D integration," *Proc. SPIE* **12496**, 124961B (2023).
2. P. Aryan, S. Sampath, and H. Sohn, "An overview of non-destructive testing methods for integrated circuit packaging inspection," *Sensors* **18**(7), 1981 (2018).
3. Y. Gao et al., "Surface third and fifth harmonic generation at crystalline Si for non-invasive inspection of Si wafer's inter-layer defects," *Opt. Express* **26**(25), 32812 (2018).
4. E. Zschech, "Nano NDE with X-Rays," in *Handbook of Nondestructive Evaluation 4.0*, N. Meyendorf, Eds., pp. 1377–1400, Springer Nature Switzerland, Cham (2025).
5. T. Gandhi, *Microelectronics Failure Analysis: Desk Reference (Seventh Edition)*, ASM International (2019).
6. A. Trigg, "Applications of infrared microscopy to IC and MEMS packaging," *IEEE Trans. Electron. Packag. Manuf.* **26**(3), 232–238 (2003).
7. G. Nádudvari et al., "Infrared optical solutions for void inspection of bonded wafers," in *IEEE 10th Electron. Syst.-Integr. Technol. Conf. (ESTC)*, IEEE, pp. 1–4 (2024).
8. J. Höglund et al., "Detection and characterization of three-dimensional interconnect bonding voids by infrared microscopy," *J. Micro/Nanolithogr., MEMS, MOEMS* **13**(1), 011208 (2014).
9. Evident, "Capabilities of near-infrared imaging for electronics and semiconductor inspection," 2023, https://evidentscientific.com/en/insights/capabilities-of-near-infrared-imaging-for-electronics-and-semiconductor-inspection (accessed 3 April 2025).
10. W. S. M. Werner et al., "Optical constants and inelastic electron-scattering data for 17 elemental metals," *J. Phys. Chem. Ref. Data* **38**(4), 1013–1092 (2009).
11. H. Yu, "Scanning acoustic microscopy for material evaluation," *Appl. Microsc.* **50**, 25 (2020).
12. S. Brand, G. Vogg, and M. Petzold, "Defect analysis using scanning acoustic microscopy for bonded microelectronic components with extended resolution and defect sensitivity," *Microsyst. Technol.* **24**(1), 779–792 (2018).
13. H. Liang, J. Xue, and K. Lu, "Image resolution enhancement method of scanning acoustic microscope for semiconductor inspection," *NDT E Int.* **154**(Nov. 2021), 103328 (2025).
14. T. H. Kim et al., "Through-silicon via device non-destructive defect evaluation using ultra-high-resolution acoustic microscopy system," *Materials* **16**(2), 860 (2023).
15. G. Busse, "Optoacoustic and photothermal material inspection techniques," *Appl. Opt.* **21**(1), 107–110 (1982).
16. P. J. S. Van Capel, E. Péronne, and J. I. Dijkhuis, "Nonlinear ultrafast acoustics at the nano scale," *Ultrasonics* **56**, 36–51 (2015).
17. P. L. M. J. Van Neer et al., "Feasibility study of photo thermal acoustic imaging of buried nanowires in Gate-All-Around Nanowire FETs," in *IEEE Int. Ultrasonics Symp. (IUS)*, Washington, DC, pp. 1–4 (2017).
18. J. Chen et al., "Nondestructive inspection of metallic microstructure chips based on photoacoustic remote sensing microscopy," *Appl. Phys. Lett.* **120**(18), 182201 (2022).
19. L. E. Kinsler et al., *Fundamentals of Acoustics*, 4th ed., John Wiley and Sons Inc. Hoboken.
20. Q. J. Wang and D. Zhu, *Hertz Theory: Contact of Spherical Surfaces BT – Encyclopedia of Tribology*, Q. J. Wang and Y.-W. Chung, Eds., pp. 1654–1662, Springer US, Boston, MA (2013).
21. P. L. M. J. van Neer et al., "Suitability of half-wavelength contact acoustic microscopy to detect deeply buried voids," *Proc. SPIE* **13426**, 134261M (2025).
22. P. L. M. J. Van Neer et al., "Feasibility of 4 GHz half wavelength contact acoustic microscopy (HaWaCAM)," in *IEEE Int. Ultrason. Symp. IUS*, IEEE, pp. 1–4 (2021).
23. R. H. Stolt, "Migration by Fourier transform," *Geophysics* **43**(1), 23–48 (1978).
24. S. F. Wang et al., "Determination of acoustic wave velocities and elastic properties for diamond and other hard materials," *Mater. Chem. Phys.* **85**(2–3), 432–437 (2004).
25. U. Gösele et al., "Wafer bonding for microsystems technologies," *Annu. Rev. Mater. Sci.* **28**, 215–241 (1998).
26. B. Yilmaz et al., "Air-coupled, contact, and immersion ultrasonic non-destructive testing: comparison for bonding quality evaluation," *Appl. Sci.* **10**(19), 6757 (2020).
27. B. A. Auld, *Acoustic Fields and Waves in Solids*, Wiley Interscience Publication, New York (1973).
28. S. Lemlikchi et al., "Direct transduction method for measuring the ultrasonic attenuation in Si(111) in the frequency range 100 MHz–1 GHz," *Measurement* **100**, 279–287 (2017).

29. R. Tabrizian, M. Rais-Zadeh, and F. Ayazi, "Effect of phonon interactions on limiting the f.Q product of micromechanical resonators," in *Proc. TRANSDUCERS 2009–2009 Int. Solid-State Sens. Actuators and Microsyst. Conf.*, Denver, CO (2009).
30. H.-J. Butt, B. Cappella, and M. Kappl, "Force measurements with the atomic force microscope: technique, interpretation and applications," *Surf. Sci. Rep.* **59**(1–6), 1–152 (2005).

Benoit A. J. Quesson graduated from the Ecole Supérieure d'Electronique de l'Ouest (ESEO) in France in 2003 with a specialty in signal processing. He is a senior scientist in the Acoustic Measurement Systems (AMS) Department of TNO (The Netherlands), where he has been working since 2003. He is the author of more than 25 patents. His current research interests include acoustic metrology and inspection for the semiconductor industry and opto-acoustic transducers. He is a member of SPIE.

Douwe M. van Willigen studied microelectronics at Delft University of Technology and received his PhD at the same university. His work focused on Application Specific Integrated Circuit (ASIC) designs for medical ultrasound and industrial flow measurement using matrix ultrasound transducers. Currently, he is a scientist for TNO, where he specializes in analog electronics, ultrasound readout systems, and GHz acoustics.

Lars Hörchens holds his engineering degree in Media Technology from Ilmenau University of Technology and his PhD in applied physics from Delft University of Technology. He has worked on acoustical imaging with a focus on nondestructive testing. After developing industrial tools for weld inspection and corrosion detection for a decade, he joined TNO to extend his field of work toward medical applications and semiconductor metrology.

Anne Maaike Gerritsma is a scientist in the Acoustic Measurement Systems Department at TNO. She obtained her MSc degree in applied physics in 2021 from Delft University of Technology. Her current research interests include opto-acoustic sensors, transducer design, and GHz acoustic metrology.

Marta Saccher obtained her MSc degree in biomedical engineering in 2019 and her PhD in MEMS ultrasound in 2024 from Delft University of Technology (TU Delft), The Netherlands. She is currently a scientist at TNO, The Netherlands, in the Acoustic Measurement Systems Department. Her research focuses on ultrasound technologies for a range of applications, including acoustic metrology and opto-acoustic sensors.

Janusz Bogdanowicz has been active in the field of semiconductor metrology for 20 years and has authored and co-authored >70 papers and one book. Today, he focuses on metrology pathfinding, which involves the analysis of the critical metrology and inspection gaps for future semiconductor technologies (logic, memory, 3D integration, …) as well as the proposal of technical solutions to tackle these upcoming challenges.

Cong Chen received her PhD in materials science from the University of New South Wales, Australia, in 2015. She was a postdoctoral researcher at the University of Tours, France, and an Adolf-Martens Fellow at BAM, Germany, working on thermoelectric materials and nondestructive testing. From 2021 to 2024, she was a senior R&D Engineer at imec, Belgium, specializing in metrology and inspection for 3D integration. She is currently a process integration engineer at Applied Materials, US.

Paul L. M. J. van Neer earned his MSc degree in biomedical engineering from TU Eindhoven (2005) and his PhD from Erasmus University Rotterdam (2010) on medical ultrasound hardware. He joined TNO in 2011, developing ultrasonic measurement systems for industry. Since 2016, he has been working in Acoustic Measurement Systems as a principal scientist. His interests include GHz acoustic metrology, sonar, flexible ultrasound transducers, opto-acoustic sensors, guided waves, nonlinear acoustics, and transducer design, leading to multiple products and spin-outs.